JOURNAL OF AIRCRAFT
Vol. 38, No. 6, November–December 2001

Rocket-Based Combined-Cycle Engine Integration on an Osculating Cone Waverider Vehicle

Timothy F. O'Brien* and Mark J. Lewis†
University of Maryland, College Park, Maryland 20742

An aerodynamic model for a rocket-based combined-cycle engine-airframe integrated vehicle using an osculating cone waverider forebody is presented. Emphasis is placed on the hypersonic portion of the vehicle trajectory, where scramjet operation occurs. An analytical model for the compression flowfield in the engine is developed, validated, and incorporated into a finite-rate chemistry engine model for hydrogen and air. Issues of off-design Mach number, angle of attack, and performance through a trajectory are addressed for a nonoptimal example vehicle. The results show that the aerodynamic performance of this class of engine-airframe integrated vehicle can be rapidly solved and incorporated into a vehicle design and trajectory code.

Nomenclature

A	=	combustor cross-sectional area, m^2
a–d, f	=	curve-fit constants
C_f	=	coefficient of friction
c_p	=	specific heat at constant pressure, J/(kg-K)
$\hat{c}_p$	=	modified specific heat at constant pressure for thermally perfect gas, J/(kg-K)
D	=	drag, N
$\mathcal{D}$	=	hydraulic diameter, m
g	=	gravitational acceleration, m/s^2
H	=	altitude, m
h	=	enthalpy per unit mass, J/kg
I_{sp}	=	specific impulse, s
L	=	lift, N
L_{mix}	=	fuel mixing length, m
M	=	Mach number
$\overline{MW}$	=	molecular weight, kg/kmol
$\overline{\overline{MW}}$	=	mixture molecular weight, kg/kmol
m	=	mass, kg
$\dot{m}$	=	mass flow rate, kg/s
Pr	=	Prandtl number
P_w	=	wetted perimeter, m
p	=	pressure, N/m^2
R_e	=	radius of the Earth, m
r	=	range in x direction, m
T	=	temperature, K
Th	=	thrust, N
U	=	velocity, m/s
x	=	axial distance, m
$\bar{x}$	=	nondimensionalized mixing distance
Y	=	mass fraction
γ	=	ratio of specific heats
γ_f	=	flight-path angle
ε	=	ratio of velocity of gas injection in the x direction over the velocity of the flowfield
ρ	=	density, kg/m^3
ϕ	=	equivalence ratio
$\dot{\omega}$	=	molar production rate, kmol/(s-m^3)

Subscripts

added	=	species added for mass/fuel injection
aw	=	adiabatic wall conditions
eff	=	effective
f	=	total fuel available
i	=	ith species
mix	=	mixing
o	=	total conditions
r	=	available for reaction
w	=	wall conditions

Received 19 October 2000; revision received 25 July 2001; accepted for publication 21 August 2001.

*Graduate Research Assistant, Department of Aerospace Engineering; genghis@eng.umd.edu. Student Member AIAA.

†Professor, Department of Aerospace Engineering; lewis@eng.umd.edu. Associate Fellow AIAA.

Introduction

EXTENSIVE research has been conducted in the past several years on integrating high-speed engines with various hypersonic vehicle configurations. Tarpley[1] incorporated an oblique detonation wave engine into a caret-wing waverider vehicle, where emphasis was placed on vehicle design that included vehicle trim. O'Neill[2] integrated a scramjet engine with a conical waverider geometry, and Takashima[3] integrated an osculating cone waverider geometry with a scramjet configuration. Both of these studies incorporated vehicle optimization to maximize such aspects as range, net thrust, etc. Recently, Starkey and Lewis[4] incorporated a wedge-derived waverider with a scramjet in the design of a box-constrained hypersonic missile.

A primary shortcoming of the engine configurations previously examined is that they are unable to generate static thrust (thrust at zero velocity) and have poor performance at low Mach numbers. Hence, some other engine system (turbofan, rocket, etc.) must be integrated into the vehicle design in order for the system to reach the high speed for which it was designed. The inclusion of any low-speed propulsion system into the vehicle design inevitably leads to increased propulsion system weight and possibly increased unused weight at high speeds.

One engine design that shows promise for operation across the full Mach-number range experienced from takeoff to hypersonic cruise or access to space is the rocket-based combined-cycle (RBCC) engine. This engine cycle allows for static thrust on takeoff and subsonic speeds using ducted rockets. The configuration transitions to a ramjet engine at higher velocity to take advantage of the high total pressure of the incoming flow. As the Mach number of the vehicle increases, the static temperature behind a normal shock wave becomes too high for the combustor wall materials, necessitating supersonic combustion in the combustor, and the engine transitions to scramjet operation. The engine transitions to pure rocket mode when the air breathing combustor no longer provides sufficient thrust. The RBCC engine model incorporated in the present vehicle design is modeled loosely on the strutjet engine designed by Aerojet.[5]

The RBCC engine allows for the design of a vehicle with the potential to travel across the full range of Mach number, from takeoff to orbital velocities. In this study, the engine-airframe integration of a hydrogen-fueled RBCC engine is presented, where emphasis is placed on the hypersonic region of flight. Vehicle and engine modeling for both on- and off-design Mach number and angle of attack are discussed. A nonoptimal example vehicle is flown along a trajectory to demonstrate the performance prediction characteristics of the models.

The overall goal of this study is the development of a full vehicle model that rapidly predicts the aerodynamics on the vehicle fuselage and inside the combustor. Rapid predictability allows for full vehicle optimization that could include trajectory analysis through the full Mach-number range. This capability allows for quick, first-order analysis of vehicle geometries, which can reduce time and cost of initial design studies.

Waverider Vehicle Design

The vehicle geometry currently under investigation is based upon a hypersonic waverider forebody. The waverider concept was initially proposed by Nonweiler[6] as an example of a high-speed reentry geometry that would have high lift coefficient. In principle, a waverider can be defined as any shape that has inviscid bow shock-wave attachment at its sharp leading edges. As a result of shock-wave attachment, the high-pressure flowfield generated from the waverider compression surface is contained underneath the vehicle. Pressure containment minimizes losses caused by pressure spillage and gives waverider shapes high lift-to-drag ratio L/D at high lift coefficient.

The entire flowfield between the waverider compression surface and the bow shock is known as a result of the inverse nature of the current waverider design. Knowledge of the compression flowfield of these geometries makes them very useful in the design of engine-airframe integrated vehicles, where accurate definition of engine inlet conditions is imperative. The flexibility of geometry definition allows for rapid vehicle design and optimization. Further, the choice of generating flowfield (wedge, cone, power law,[7] etc.) offers flexibility in the vehicle design.

The waverider generation method selected for this study is the osculating cone method, proposed by Sobieczky et al.[8] The predicted aerodynamics of the shapes generated by this method have been shown to be accurate in computational studies.[9] The method is flexible enough that in addition to its unique set of shapes, given the proper values, it can generate wedge and conical waveriders. This ability is quite useful; the osculating cone method can take advantage of both the flow uniformity aspects of wedge-derived waveriders, as well as the usable volume qualities of conically derived waveriders. Providing such a wide variety of vehicle possibilities allows for a diverse optimization of the design space for various objective functions.

The vehicle configuration used in this study is largely based on the scramjet-powered vehicle designs proposed and numerically validated by Takashima,[3] a representative example of which is shown in Fig. 1 for a design Mach number of 10. The proposed vehicle design features an osculating cone waverider forebody blended into an aft section that ends with base closure at the trailing edge. The forebody has a planar portion at the centerline that generates a uniform wedge flowfield, which traverses a series of three wedge compression ramps of equal compression angle before entering the combustor. The flowfield on both the upper and lower surface aft of the forebody is predicted using shock-expansion theory. The flowfield on the nozzle portion following the combustor is computed using the method of characteristics[10] assuming two-dimensional flow with no chemical reactions. The top surface of the waverider forebody is assumed to be aligned parallel with the freestream, while the section aft of the forebody is allowed to vary, providing a slight expansion on the upper surface, giving additional lift to the vehicle. All boundary layers on the vehicle are assumed to be turbulent as a conservative estimate for the viscous drag. Vehicle mass is calculated by assuming a fuel volume fraction of 55% and assuming an average vehicle density of 136.51 kg/m^3 for the remaining 45% (Ref. 2).

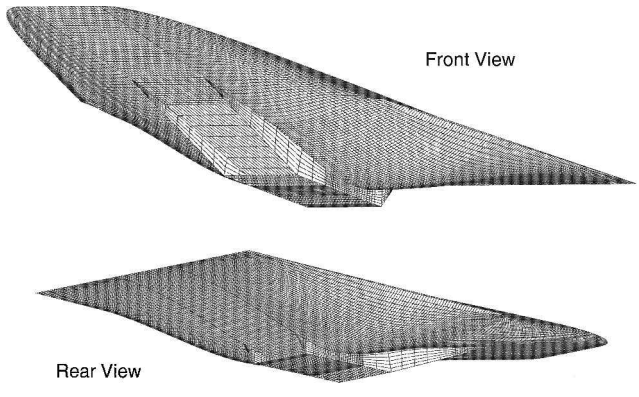

Fig. 1 Two view of example vehicle geometry ($M = 10$).

RBCC Engine Model

The RBCC engine model in this study is loosely based on published descriptions of Aerojet's strutjet engine concept.[5] The centerline and top view of the engine flowpath in scramjet mode are shown in Fig. 2. The engine is composed of a set of strut injectors at the inlet of the engine, followed by a constant-area combustor section within the struts and ending with a constant angle expansion section. The injectors act as fuel-rich rockets at subsonic speeds to entrain incoming air from the inlet, thus raising the engine's specific impulse I_{sp} compared to rocket-only operation. At transonic-supersonic speeds the struts act as isolators slowing the supersonic incoming air to subsonic speeds. In this speed regime the engine transitions from a fuel-rich rocket to a ramjet configuration. At high supersonic through hypersonic speeds, the struts act as normal fuel injectors, as well as isolators. The incoming flow is divided into smaller cross sections, so that mixing of the fuel and the air is more efficient. Splitting the incoming flow also has the effect of reducing the length of the isolator section.[11]

Examining the side view of the combustor flowpath in Fig. 2, the forebody shock and the inlet ramp shocks all meet at the engine cowl at on-design conditions. The reflected shock off the engine cowl is canceled out on the upper wall of the engine. The RBCC struts are located immediately behind the shock cancellation region and are contained entirely within the combustor (problems with inlet starting at lower speeds are not currently considered). Following the struts, a constant angle expansion section leads to the internal and external nozzle sections.

The analytical strut inlet model consists of a calculation of the interaction between two struts. The side walls of the combustor

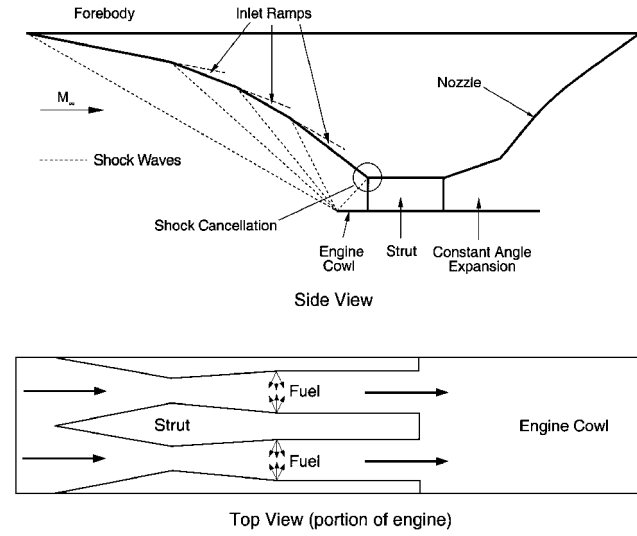

Fig. 2 RBCC engine geometry in scramjet mode, side and top view (not to scale).

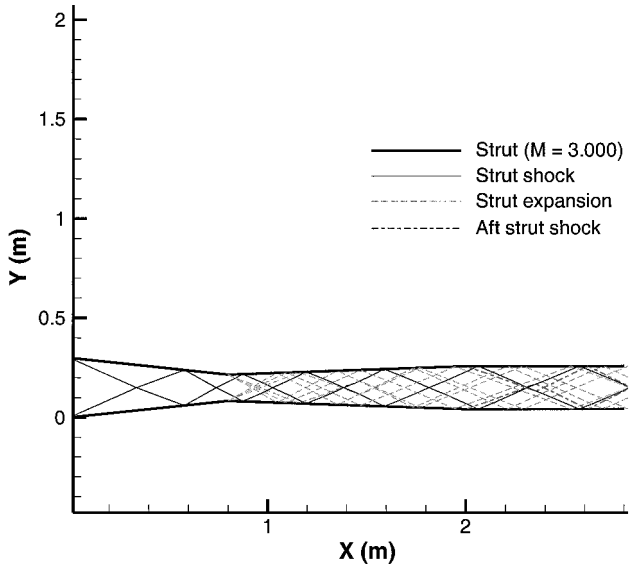

Fig. 3 Analytical solution to strut/strut interaction ($M = 3$).

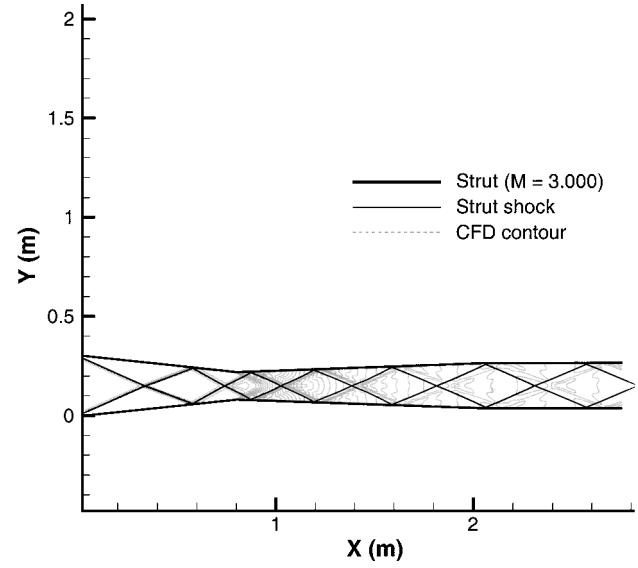

Fig. 4 Analytical solution to strut/strut interaction superimposed upon pressure contours of computational fluid dynamics solution ($M = 3$).

are assumed to be half an injector each to simplify calculations. The flowfield is also assumed to be fully two-dimensional (no flow spillage) and inviscid, thus shock-wave/boundary-layer interactions (which can be quite significant) are neglected.

The analytical solution to the strut/strut interaction is shown in Fig. 3. The solution is calculated for an incoming Mach number of three. Shock properties are calculated using the oblique shock relations. The continuous expansion fans are modeled as three discontinuous expansion waves, where properties across each wave are calculated using the Prandtl–Meyer relation. Two types of wave interaction are identified: interaction of waves of opposite family and interaction of waves of the same family. Opposite family interactions involve waves that have angles of incidence that are opposite in sign. Same family interactions involve waves that have angles of incidence that are the same in sign. Three wave interactions are calculated for each family: shock/shock, shock/expansion, and expansion/expansion. For each interaction the flow behind each wave following the interaction is iterated to find the properties that lead to the same pressure and flow direction. For shock/shock interactions of the same family, the resulting flowfield usually yields a shock and an expansion fan. In this case one of the shocks are converted to a single discontinuous expansion wave, and the wave continues to move through the combustor interacting as an expansion wave. In this fashion the flowfield wave structure throughout the entire strut cross section can be found.

The analytical model was validated by computationally solving the two-dimensional flowfield using the General Aerodynamic Simulation Program (GASP) v3.0 (Ref. 12). GASP solves the integral form of the unsteady Reynolds-averaged Navier–Stokes (RANS) equations in three dimensions subject to boundary and initial conditions. The inviscid, steady flowfield is calculated from the Euler equations (a subset of RANS) with no chemical reactions and space marching in the axial direction.

The analytical solution for the strut compression flowfield is superimposed upon a computational solution for pressure at an incoming Mach number of 3 in Fig. 4. Only the shocks emanating from the beginning of the struts are tracked through the length of the compression region. It is seen that the analytical prediction for the shock lags a little behind the computational solution in Fig. 4. This mismatch in solution is caused by the limited discretization of the expansion fans and is seen to be the initial point of error in the shock location between the two solutions.

A comparison of the computational results for area averaged exit pressure are compared to the analytical model for the strut-strut interaction in Fig. 5. The same geometry is solved for an incoming pressure of 1 atm and a wide range of inlet Mach numbers. Also plotted in Fig. 5 is the prediction using quasi-one-dimensional

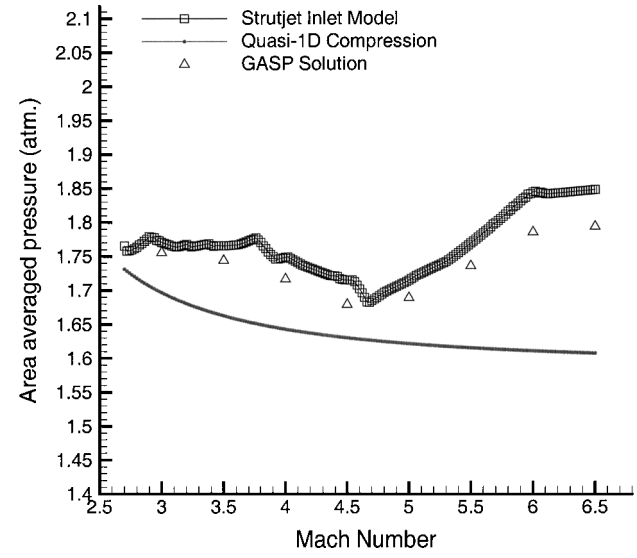

Fig. 5 Area averaged exit pressure vs Mach number for strut/strut interaction.

flow analysis. The analytical model correctly predicted the pressure vs Mach number trend found from the computational solution, but slightly overpredicts the pressure for all Mach numbers. The maximum error in pressure overprediction was found to be approximately 3%. This error can be attributed to the limited number of discontinuous waves discretizing the continuous expansion fan. The error in pressure was deemed acceptable considering the additional computational costs involved in further discretizing the expansion fan, and errors inherent to the model for neglecting shock-wave/boundary-layer interactions.

The flowfield through the combustor and expansion region is modeled with the following assumptions: steady-state conditions, quasi-one-dimensional flow, normal fuel injection of hydrogen, and a thermally perfect gas. The incoming flow to the engine is assumed to be the area-averaged quantities solved from the analytical model for the strut/strut interaction (Fig. 3). The flowfield model is expressed by the following governing equations (based on derivations by Shapiro[13] and Turns[14]) developed and validated by O'Brien et al.[15]:

$$\frac{1}{\dot{m}}\frac{\mathrm{d}\dot{m}}{\mathrm{d}x} = \frac{1}{\rho}\frac{\mathrm{d}\rho}{\mathrm{d}x} + \frac{1}{U}\frac{\mathrm{d}U}{\mathrm{d}x} + \frac{1}{A}\frac{\mathrm{d}A}{\mathrm{d}x} \tag{1}$$

$$\frac{1}{p}\frac{\mathrm{d}p}{\mathrm{d}x} + \frac{\gamma M^2}{2U^2}\frac{\mathrm{d}U^2}{\mathrm{d}x} + \frac{2\gamma M^2 C_f}{\mathcal{D}} + \frac{\gamma M^2(1-\varepsilon)}{\dot{m}}\frac{\mathrm{d}\dot{m}}{\mathrm{d}x} = 0 \tag{2}$$

$$\frac{\mathrm{d}Y_i}{\mathrm{d}x} = \frac{\dot{\omega}_{i,\mathrm{mix}} MW_i}{\rho U} + \frac{1}{\dot{m}}\frac{\mathrm{d}\dot{m}_{i,\mathrm{added}}}{\mathrm{d}x} - \frac{Y_i}{\dot{m}}\frac{\mathrm{d}\dot{m}}{\mathrm{d}x} \tag{3}$$

$$\frac{\mathrm{d}\overline{MW}}{\mathrm{d}x} = -\overline{MW}^2\left(\sum_i \frac{1}{MW_i}\frac{\mathrm{d}Y_i}{\mathrm{d}x}\right) \tag{4}$$

$$\frac{1}{p}\frac{\mathrm{d}p}{\mathrm{d}x} = \frac{1}{\rho}\frac{\mathrm{d}\rho}{\mathrm{d}x} + \frac{1}{T}\frac{\mathrm{d}T}{\mathrm{d}x} - \frac{1}{\overline{MW}}\frac{\mathrm{d}\overline{MW}}{\mathrm{d}x} \tag{5}$$

$$\frac{\mathrm{d}T}{\mathrm{d}x} = \frac{1}{\hat{c}_p}\left[-\sum_i h_i\frac{\mathrm{d}Y_i}{\mathrm{d}x} + \frac{1}{\dot{m}}\sum_i\left(h_i\frac{\mathrm{d}\dot{m}_i}{\mathrm{d}x}\right)_{\mathrm{added}} - \frac{2C_f c_p(T_{\mathrm{aw}} - T_w)}{Pr^{\frac{2}{3}}\mathcal{D}A} - \frac{h_o}{\dot{m}}\frac{\mathrm{d}\dot{m}}{\mathrm{d}x} - U\frac{\mathrm{d}U}{\mathrm{d}x}\right] \tag{6}$$

Equations (1–6) are the differential forms of continuity, momentum, species conservation, mixture molecular weight, equation of state, and energy, respectively. The engine model requires a user-defined area profile $\mathrm{d}A/\mathrm{d}x$, mass addition profile $\mathrm{d}\dot{m}/\mathrm{d}x$, fuel availability for reaction profile (assumed to be the same as $\mathrm{d}\dot{m}/\mathrm{d}x$ in this study), and viscous model.

The area profile assumes a constant area between the struts, followed by a finite expansion from the base of the strut, followed by a constant angle expansion until the nozzle has been reached. The base pressure on the strut is assumed to be an average of the pressure before and after the expansion. The normal injection hydrogen mass mixing profile (discussed in detail in Ref. 15) is given as

$$\frac{\mathrm{d}\dot{m}}{\mathrm{d}x} = \frac{\dot{m}_r}{L_{\mathrm{mix}}}\left[\frac{cd\bar{x}^2 + (bd + cf - d)\bar{x} + bf}{\bar{x}(d\bar{x} + f)}\right] \tag{7}$$

where the mass flow rate available for reaction is

$$\dot{m}_r = \dot{m}_f\frac{a\bar{x}^b\exp(c\bar{x})}{d\bar{x} + f} \tag{8}$$

$$\bar{x} \equiv \frac{x}{L_{\mathrm{mix}}} \tag{9}$$

Fuel injection is assumed to begin at the end of the expansion portion of the strut/strut flowfield (see Fig. 2). The mixing length is set to the length of the constant-area portion between the struts (2.6 m), the mixing efficiency is assumed to be 95%, and the curve-fit constants[15] are $a = 1.1703$, $b = 0.62925$, $c = 0.42632$, $d = 1.4615$, and $f = 0.32655$. The friction coefficient C_f is calculated using Eckert's turbulent reference temperature method,[16] where the viscosity is calculated using Sutherland's law. The hydraulic diameter is defined as

$$\mathcal{D} \equiv 4A/P_w \tag{10}$$

The adiabatic wall temperature is calculated by

$$T_{\mathrm{aw}} = T\left\{1 + Pr^{\frac{1}{3}}[(\gamma - 1)/2]M^2\right\} \tag{11}$$

where the Prandtl number is assumed to have a constant value of 0.71.

Equations (1–6) are a stiff set of ordinary differential equations (ODEs) because of the chemical production terms from combustion. Solution of these equations requires a stiff ODE solver, which can account for the differing timescales. A detailed discussion of the solution of these equations is provided in Ref. 15. The solver used in this study was VODPK.[17] VODPK integrates the set of stiff ODEs using a backward differentiation formula. Chemical information such as molecular weight, specific heat, and reaction rates is provided by CHEMKIN-II.[18]

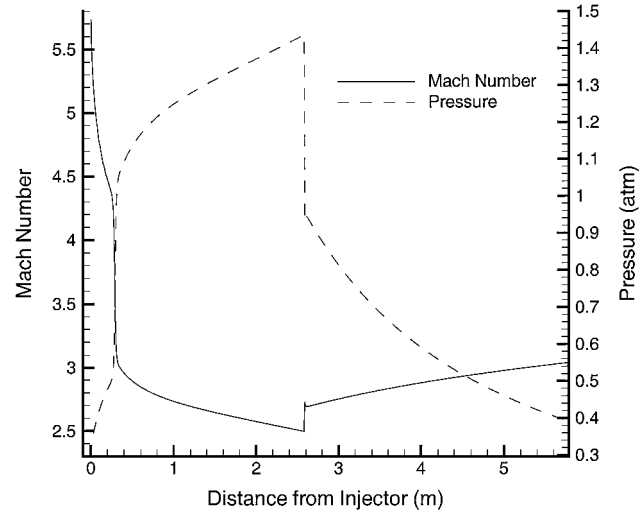

Fig. 6 Mach number and pressure distribution in example RBCC engine.

The ambient air composition is 78% nitrogen, 21% oxygen, and 1% argon by volume, and is assumed to remain constant through all flowfield compression prior to the combustor. The hydrogen/air reaction mechanism used in this study was proposed by Jachimowski.[19] Jachimowski's mechanism contains 14 species and 33 reactions and includes nitrogen chemistry.

An example combustor flowfield pressure and Mach-number distribution is shown in Fig. 6. The incoming combustor conditions are assumed to be $p = 0.3$ atm, $T = 980$ K, $M = 5.73$, $\gamma = 1.34$, $\dot{m} = 722$ kg/s, $\phi = 1$, $T_w = 1200$ K (assumed), combustor expansion length of 3.17 m, and a combustor expansion angle of 8.9 deg. Details of the engine flowfield are discussed in Ref. 15. In Fig. 6 the Mach number is seen to decrease at the beginning of the combustor because of mass addition. At an axial distance of about 0.25 m, fuel ignition occurs, resulting in a rapid decrease in Mach number. Following fuel ignition, the Mach number is seen to continually decrease because of combustion and viscous effects, until the end of the struts are reached. The flow then rapidly expands because of the base of the struts and then continues to expand through the constant angle expansion, resulting in an increase in Mach number.

Off-Design Conditions and Trajectory Performance

An important aspect of the performance of the vehicle is its off-design aerodynamics for both angle of attack and Mach number. The hypersonic, off-design aerodynamic performance for the waverider forebody is calculated using a quadratic interpolation between tangent-wedge and tangent-cone theory proposed by Bowcutt and reported by Grantz.[20] This method is modified for the present study by using the exact solution for tangent wedge and tangent cone instead of the approximate relations given in Ref. 20. Solutions based on this method were numerically validated for both angle of attack and Mach number by Takashima.[3] Calculation of the flowfield over the remaining vehicle is then performed using the same methods already discussed, with the exception of the forebody upper surface and the engine cowl. The upper surface of the forebody is assumed to be wedge flow for negative angles of attack and Prandtl–Meyer flow for positive angles of attack.

The location of shock waves generated by the forebody and the inlet ramps will shift for off-design angle of attack and Mach number. If not properly accounted for, the shifted shock waves could enter into the engine, causing severe shock wave boundary-layer interactions, localized heating, and boundary-layer separation. To avoid this, a constraint is imposed upon the design such that the engine cowl is always positioned to prevent any shocks from being swallowed into the engine. The engine cowl is allowed to translate axially to move the engine cowl shock such that it cancels on the upper surface of the engine. If an inlet interaction occurs such that an expansion off of the last shock interaction will enter the engine,

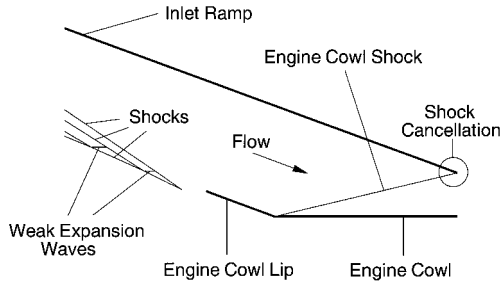

Fig. 7 Inlet lip geometry.

a "lip" is added to the inlet to prevent any nonuniformities from entering the engine (see Fig. 7). Any vehicle that violates the shock swallowing constraint is not considered. It is acknowledged that the inlet lip concept can, in reality, be mechanically infeasible or have a large weight. However, compared to other methods of regulating the inlet flowfield (i.e., moving inlet ramps, etc.) this method was deemed acceptable for the current study.

Knowledge of flowfield properties over the entire vehicle for a range of Mach numbers and angles of attack allows for performance calculations of the vehicle as a whole along a flight trajectory. The trajectory model for a nonrotating spherical Earth with the range in the axial (x) direction as the dependent variable[21] is

$$\frac{\mathrm{d}H}{\mathrm{d}r} = \tan\gamma_f\left(1+\frac{H}{R_e}\right) \tag{12}$$

$$\frac{\mathrm{d}\gamma_f}{\mathrm{d}r} = \left(\frac{L-mg\cos\gamma_f}{mU^2\cos\gamma_f}+\frac{1}{R_e+H}\right)\left(1+\frac{H}{R_e}\right) \tag{13}$$

$$\frac{\mathrm{d}U}{\mathrm{d}r} = \left(\frac{Th-D-mg\sin\gamma_f}{mU\cos\gamma_f}\right)\left(1+\frac{H}{R_e}\right) \tag{14}$$

$$\frac{\mathrm{d}m}{\mathrm{d}r} = -\frac{\dot{m}}{U\cos\gamma_f}\left(1+\frac{H}{R_e}\right) \tag{15}$$

The performance is calculated by assuming a known trajectory profile (H vs r) and then integrating the preceding equations to solve for the change in the flight-path angle, the change in the velocity, and the change in mass of the vehicle.

Results

The preceding models for the vehicle and engine are demonstrated by application to a Mach 12 vehicle shown in Fig. 8. The geometry is selected as an example to demonstrate the capabilities of the model to predict performance and does not imply an optimum solution. The example also does not include moment trim; thus, the effects of control surfaces on the performance of the vehicle are not accounted. The geometric properties for the example vehicle are shown in Table 1. All performance numbers assume a constant value for the equivalence ratio.

The L/D and effective specific impulse $I_{sp_{eff}}$ are plotted as functions of Mach number and angle of attack in Figs. 9 and 10, respectively. The Mach 8 solution has a lower angle-of-attack limit to ensure compression on the lower surface of the forebody. The Mach 10 and 12 solutions have a lower angle-of-attack limit to ensure that no shocks are swallowed into the engine.

One noticeable trait of these vehicles is the difference in the derivative of lift-to-drag ratio with respect to angle of attack. The vehicle has a much steeper slope in lift-to-drag ratio at negative angles of attack than for positive angles of attack. This trend is caused by shock compression on the upper surface for negative angles of attack, thus lowering the overall lift of the vehicle and L/D. For positive angles of attack, pressure drag on the lower surface is the prime contributor to lowering the L/D.

Figure 10 shows that, for a limited range of angle of attack, the vehicle has positive net thrust (i.e., positive $I_{sp_{eff}}$) for a range of Mach

Table 1 Mach 12 example vehicle properties

Property	Value
Length, m	76.8
Width, m	20.5
Height, m	5.2
Volume, m^3	2392
Planform area, m^2	429.2
Max cross-sectional area, m^2	71.6
Inlet ramp angles, deg	1.07
Shock angle, deg	9.26
Equivalence ratio	1

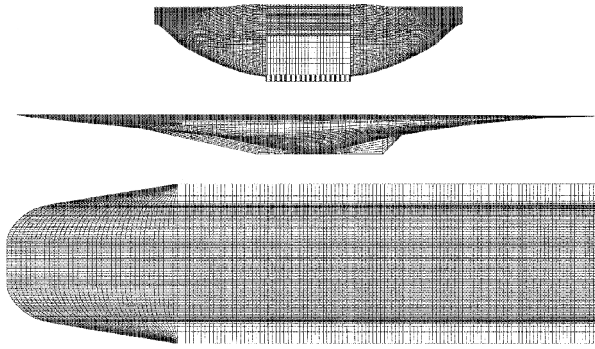

Fig. 8 Three view of Mach 12 example vehicle.

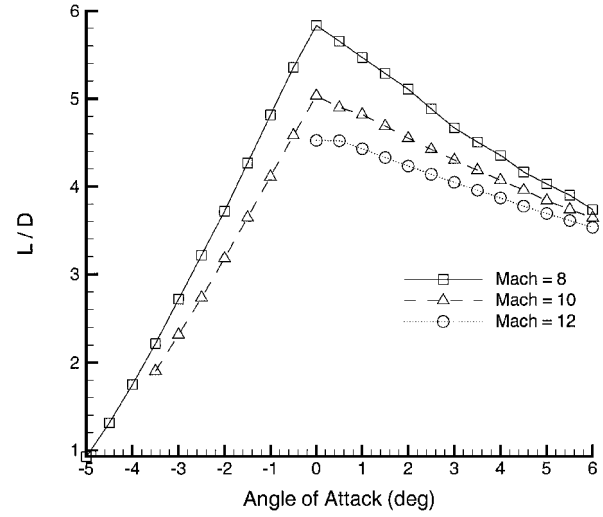

Fig. 9 L/D vs angle of attack for example Mach 12 vehicle ($\phi = 1$).

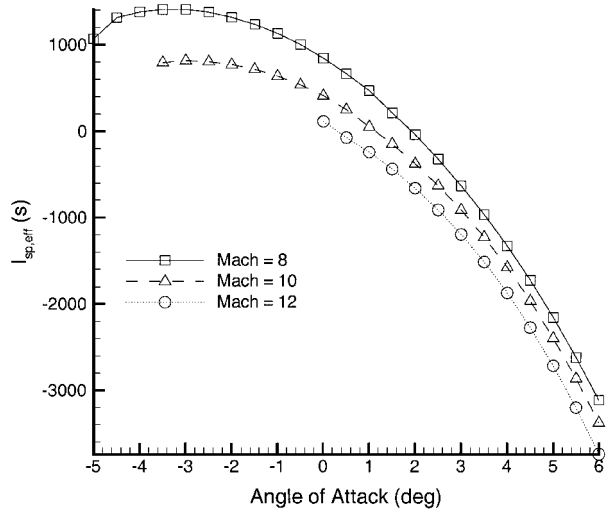

Fig. 10 $I_{sp_{eff}}$ vs angle of attack for example Mach 12 vehicle ($\phi = 1$).

number between 8 and 12. High $I_{sp_{eff}}$ at negative angle of attack is primarily caused by the lift vector being shifted in the direction of thrust. This effect has its limits because the increased pressure on the upper surface as a result of shock compression increases the overall drag of the vehicle. Also, as angle of attack gets more negative less compression occurs prior to entering the engine, and less mass is captured by the engine inlet, resulting in a lower thrust from the engine.

The example vehicle was flown through a nonoptimal, quadratic trajectory as shown in Fig. 11. Starting conditions for the vehicle were an altitude of 30.7 km, a Mach number of 8, and a constant equivalence ratio of 1. Two cases were run for the given trajectory, corresponding to a vehicle with 40% of its fuel remaining at the beginning of the trajectory and one with 50% of its fuel remaining. The resulting velocity profile for each case is also plotted in Fig. 11. The difference in starting mass resulted in a 1% increase in velocity over the given trajectory. For both cases shown the vehicle continued to accelerate through the entire given trajectory.

The Mach-number profile for the example vehicle is shown in Fig. 12. The 40% fuel remaining case resulted in a final Mach number of 9.75 while the 50% case resulted in a final Mach number of 9.65. The angle-of-attack profile is also presented in Fig. 12. For both cases a maximum in angle of attack was found at a range location near 1550 km. The deviation in angle of attack across the trajectory was seen to be quite small (~0.3 deg). This region of angle of attack is seen to be close to the maximum $I_{sp_{eff}}$ for Mach

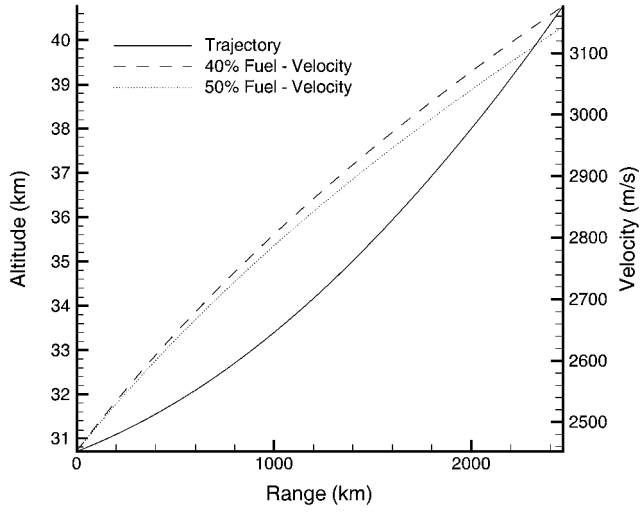

Fig. 11 Trajectory and velocity profile of example vehicle as a function of range and percent fuel remaining.

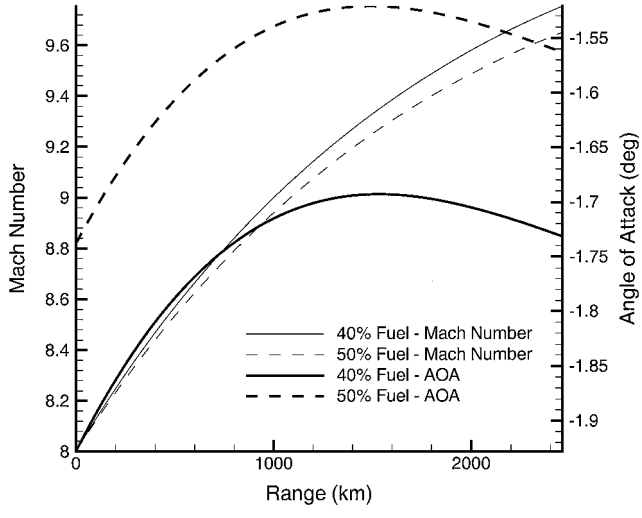

Fig. 12 Mach number and angle-of-attack profile of example vehicle as function of range and percent fuel remaining.

numbers between 8 and 10 (see Fig. 10) and to have a relatively constant value of L/D between 3.5 and 4 (see Fig. 9). The fuel mass consumed for the 40% case was 14,273 kg of H_2 compared with 14,552 kg of H_2 for the 50% case for the same trajectory. Because the 40% case had less fuel, it had to do less work to get to the same altitude as the 50% case, hence having lower fuel consumption. For both cases that the vehicle and trajectory are nonoptimal.

Conclusions

An aerodynamic model for an RBCC engine-airframe integrated vehicle has been presented. The RBCC model includes the two-dimensional inviscid compression flowfield between struts, as well as finite-rate hydrogen/air chemistry in the combustor section. Off-design performance including Mach number and angle of attack is considered and incorporated into the model. A nonoptimal example Mach 12 vehicle was presented and flown through a given trajectory to calculate its performance for two cases (40 and 50% fuel remaining at altitude).

The methodology presented herein is particularly useful for initial design studies, trajectory analyses, and/or optimizations. These applications are dependent on the time needed to calculate the aerodynamic forces on the vehicle geometry. The resulting analyses will benefit if the forces on the vehicle can be calculated both quickly and accurately. The vehicle and engine methods provided herein give detailed aerodynamics both on the vehicle fuselage and within the engine (including thermochemistry considerations) and do so in less than a CPU second on a typical sun workstation.

Improvements to the vehicle model would include control surfaces to trim out the vehicle and to incorporate control surface losses to the vehicle lift and drag calculations. Another addition to the vehicle model will be a compression surface on the top surface of the waverider forebody to increase volume. The next step in the vehicle model development is aerodynamic prediction of the flowfield on the fuselage and in the combustor for flight speeds far from design. Subsonic, transonic, and low supersonic flight Mach numbers will play a key role in the overall design of an engine-airframe integrated vehicle designed for a takeoff to orbit mission. Predicting these flowfields rapidly and reliably is vital for a full trajectory analysis of vehicle flight performance.

Additions to the engine model will include an improved mixing model over the curvefit currently presented. Also, the additional modes of ramjet and rocket will be added into the engine-airframe integration. Finally, the current model allows for the use of other fuel types in the vehicle design, so long as a reaction mechanism is provided. Future work could include hydrocarbon fuels and their effects on the vehicle design.

Acknowledgments

This research was supported by Lockheed Martin Skunk Works and by NASA John H. Glenn Research Center at Lewis Field, Ohio. Technical monitors for this research were Robert Boyd and Mary Hudson of the Airbreathing Hypersonics Advanced Programs department at Lockheed Martin at Palmdale, CA, and Don Palac at NASA John H. Glenn Research Center. The authors would like to thank Ryan Starkey of the University of Maryland, College Park, Maryland, for his assistance in developing the combustor model and Lael Rudd of the University of Maryland for his assistance on the trajectory calculations. Thanks also go to Adam Siebenhaar and Mel Bulman from Aerojet for their contributions.

References

[1] Tarpley, C., "The Optimization of Engine—Integrated Hypersonic Waveriders with Steady State Flight and Static Margin Constraints," Ph.D. Dissertation, Dept. of Aerospace Engineering, Univ. of Maryland, College Park, May 1995.

[2] O'Neill, M. K. L., "Optimized Scramjet Engine Integration on a Waverider Airframe," Ph.D. Dissertation, Dept. of Aerospace Engineering, Univ. of Maryland, College Park, Aug. 1992.

[3] Takashima, N., "Optimization of Waverider—Based Hypersonic Vehicle Designs," Ph.D. Dissertation, Dept. of Aerospace Engineering, Univ. of Maryland, College Park, May 1997.

[4]Starkey, R. P., and Lewis, M. J., "Sensitivity of Hydrocarbon Combustion Modeling on Hypersonic Missile Design," AIAA Paper 2000-3312, July 2000.

[5]Siebenhaar, A., and Bulman, M., "The Strutjet Engine: The Overlooked Option for Space Launch," AIAA Paper 95-3124, July 1995.

[6]Nonweiler, T. R. F., "Aerodynamic Problems of Manned Space Vehicles," *Journal of the Royal Aeronautical Society*, Vol. 63, No. 585, Sept. 1959, pp. 521–528.

[7]Sabean, J., Lewis, M., Mee, D., and Paull, A., "Performance Study of a Power Law Starbody," *Journal of Spacecraft and Rockets*, Vol. 36, No. 5, 1999, pp. 646–652.

[8]Anderson, J. P., Lewis, M. J., Sobieczky, H., Dougherty, F., and Jones, K., "Hypersonic Waverider Design from Given Shock Waves," *Proceedings of the First International Hypersonic Waverider Symposium*, edited by J. D. Anderson and M. J. Lewis, Univ. of Maryland, College park, MD, Oct. 1990.

[9]Takashima, N., and Lewis M., "Navier–Stokes Computation of a Viscous Optimized Waverider," *Journal of Spacecraft and Rockets*, Vol. 31, No. 3, 1994, pp. 383–391.

[10]Anderson, J. D., *Modern Compressible Flow: with Historical Perspective*, McGraw–Hill, New York, 1990, pp. 282–289.

[11]Heiser, W., and Pratt, D., *Hypersonic Airbreathing Propulsion*, AIAA, Washington, DC, 1994, pp. 251–257.

[12]McGrory, W., Slack, D., Applebaum, M., and Walters, R., GASP Version 3.0. Aerosoft, Inc., Blacksburg, VA, 1996.

[13]Shapiro, A., *The Dynamics and Thermodynamics of Compressible Fluid Flow*, Vol. 1, Ronald Press Co., New York, 1953, pp. 226–231.

[14]Turns, S. R., *An Introduction to Combustion*, McGraw–Hill, New York, 1996, pp. 83–138.

[15]O'Brien, T. F., Starkey, R. P., and Lewis, M. J., "A Quasi-One-Dimensional High-Speed Engine Model with Finite-Rate Chemistry," *Journal of Propulsion and Power*, Vol. 17, No. 6, 2001, pp. 1366–1374.

[16]Eckert, E. R. G., "Engineering Relations for Friction and Heat Transfer to Surfaces in High Velocity Flow," *Journal of the Aeronautical Sciences*, Vol. 22, 1955, pp. 585–587.

[17]Byrne, G. D., Hindmarch, A. C., and Brown, P. N., "VODPK: Variable-Coefficient Ordinary Differential Equation Solver with the Preconditioned Krylov Method GMRES for the Solution of Linear Systems," Lawrence Livermore National Lab., Livermore, CA, 1997.

[18]Kee, R. J., Rupley, F. M., and Miller, J. A., "CHEMKIN-II: A Fortran Chemical Kinetics Package for the Analysis of Gas Phase Chemical Kinetics," SAND 89-8009B, Sandia Natl. Lab., Albuquerque, N.M., 1989.

[19]Jachimowski, C. J., "An Analytical Study of the Hydrogen-Air Reaction with Application to Scramjet Combustion," NASA TP 2791, Feb. 1988.

[20]Grantz, A., "Calibration of Aerodynamic Engineering Methods for Waverider Design," AIAA Paper 94-0382, Jan. 1994.

[21]Chuang, C., and Morimoto, H., "Periodic Optimal Cruise for a Hypersonic Vehicle with Constraints," *Journal of Spacecraft and Rockets*, Vol. 34, No. 2, 1997, pp. 165–171.